Chem. Mater. **2005,** *17,* 6327−6337

Electrochemical Reactivity and Design of NiP_2 Negative Electrodes for Secondary Li-Ion Batteries

F. Gillot,[†] S. Boyanov,[‡] L. Dupont,[†] M.-L. Doublet,[§] M. Morcrette,[†] L. Monconduit,[*,‡] and J.-M. Tarascon[†]

LRCS, UMR 6007, Université de Picardie Jules Verne, 80039 Amiens, France, and
LAMMI, UMR 5072, Université Montpellier II, 34095 Montpellier, France, and
LSDSMS, UMR 5636, Université Montpellier II, 34095 Montpellier, France

Received July 19, 2005. Revised Manuscript Received September 23, 2005

We report the electrochemical study of cubic and monoclinic NiP_2 polymorphs toward Li, as a candidate for anodic applications for Li-ion batteries. We found that the monoclinic form is the most attractive one performance-wise. Monoclinic NiP_2 can reversibly uptake 5 lithium per formula unit, leading to reversible capacities of 1000 mAh/g at an average potential of 0.9 V vs Li^+/Li°. From complementary X-ray diffraction (XRD) and HRTEM (high-resolution transmission electron microscopy) measurements, it was shown that, during the first discharge, the cubic phase undergoes a pure conversion process ($NiP_2 + 6\,Li^+ + 6e^- \rightarrow Ni^\circ + 2Li_3P$) as opposed to a sequential insertion−conversion process for monoclinic NiP_2. Such a different behavior rooted in subtle structural changes was explained through electronic structure calculations. Once the first discharged is achieved, both phases were shown to react with Li through a classical conversion process. More importantly, we report a novel way to design NiP_2 electrodes with enhanced capacity retention and rate capabilities. It consists in growing the monoclinic NiP_2 phase, through a vapor-phase transport process, on a commercial Ni-foam commonly used in Ni-based alkaline batteries. These new self-supported electrodes, based on chemically made interfaces, offer new opportunities to fully exploit the capacity gains provided by conversion reactions.

1. Introduction

Fifteen years after their first commercialization, rechargeable Li-ion batteries are widely accepted and are becoming the main power source in today's portable electronics. They are even considered as serious candidates to power future hybrid electric vehicles (HEVs) and, in the long run, EVs. Because of its advent on the market, such technology has been using a layered oxide ($LiCoO_2$) as positive electrode and a carbonaceous material as negative electrode, both reacting toward Li through insertion/de-insertion reactions. Improvements capacity-wise and energy-wise were rather the results of engineering than chemistry advances. The latter is low owing to the difficulty encountered in designing either positive materials that can react with more than one Li per 3d metal or negative electrodes showing greater capacities than graphite while maintaining an excellent capacity retention. Driven by EV market demands, namely in terms of volume restriction, researchers have focused their attention on the search for either (i) high-voltage redox systems (e.g., highly oxidant positive electrode materials) so that fewer cells will be required for a predefined application voltage or (ii) high-energy density systems by increasing the volumetric capacity of either the positive or negative electrode in order to reduce the size of each cell and, therefore, of the overall stack. Regarding negative electrodes, the most promising candidates have long been the metal elements capable of forming alloys with Li, such as Si (4200 mAh/g)[1] or Sn (1200 mAh/g).[2] Owing to the poor efficiency of the Li alloying/de-alloying process leading to poor long-term stability, none of these electrodes had been used in practical cells yet. Such a long-lasting limitation is at the verge of being overcome in light of some recent reports on Si-embedded nanoparticle electrodes[3] and SONY's recent announcement regarding the launching of Nexelion, which uses an Sn-based nanocomposite negative electrode.[4]

Five years ago, searching for the benefits that nanomaterials could bring to the field of electrode materials, it was with great surprise that we unravelled that simple oxides can electrochemically react toward Li, leading to sustainable reversible capacities as high as 900 mAh/g.[5] These results were explained by the following conversion reaction: $M_xO_y + 2ye^- + 2yLi^+ \leftrightarrows xM^0 + yLi_2O$. It was later demonstrated that this new Li reactivity mechanism was not specific to oxides but could also be found with sulfides, nitrides, fluorides, and phosphides.[6−9] As compared to the classical insertion reactions that govern the energy stocked in the

---

[*] Corresponding author e-mail: moncondu@univ-montp2.fr.
[†] LRCS, Université de Picardie Jules Verne.
[‡] LAMMI, Université Montpellier II.
[§] LSDSMS, Université Montpellier II.

(1) Huggins, R. A. *J. Power Sources* **1999**, *13*, 81.
(2) Besenhard, J. O.; Yang, J.; Winter, M. *J. Power Sources* **1997**, *68*, 87.
(3) Kushida, K.; Kuriyama, K.; Nozaki, T. *Appl. Phys. Lett.* **2002**, *81* (26), 5068.
(4) Sony Corp. Information, Feb 15, 2005. http://www.sony.net/SonyInfo/News/Press/.
(5) Poizot, P.; Laruelle, S.; Grugeon, S.; Dupont, L.; Tarascon, J.-M. *Nature* **2000**, *407*, 496.
(6) Grugeon, S.; Laruelle, S.; Dupont, L.; Tarascon, J.-M. *Solid State Sci.* **2003**, *5*, 895.

10.1021/cm051574b CCC: $30.25

actual Li-ion batteries, and which are limited to $1e^-$ or even $0.5e^-$ per 3d metal atom ($LiCoO_2$), these new conversion reactions that can involve $2e^-$ or more (per 3d metal atom) were thought of as a new means to enable the creation of a new class of electrodes with staggering capacity gains over various voltage ranges depending on the nature of the X anion.

Therefore, as research on these new electrodes proceeded, we rapidly experienced that, if we ever wanted to fully utilize conversion reactions in practical cells, we needed to (1) enhance their poor kinetics that result in a large polarization and, hence, a poor energy efficiency, (2) improve their capacity retention upon cycling, and (3) find chemical ways to lower and narrow their voltage reactivity range toward Li. A few of these challenges have already been successfully addressed. Kinetic improvements in conversion reactions together with an enhancement of their capacity retention were achieved by either (1) acting at the particle surfaces through the use of conducting coatings as reported by Hu et al. for carbon-coated Cr_2O_3 particles,[10] (2) moving from bulk to thin-film material as illustrated by the studies by Pralong et al. on Co_3O_4 thin films,[11] or (3) playing with new electrode design. For instance, we recently reported on a new electrode configuration that consists of the high temperature growth of an electrochemical oxide layer at the surface of a stainless steel current collector. Owing to this chemically made current collector/active material interface, the electrode shows an outstanding capacity retention (>800 cycles) and good kinetics (90% of the full capacity at 1C). Therefore, such electrodes still suffer from a large polarization (~0.8 V) that is intrinsic to conversion reactions and linked, among others, to the electrical energy needed to overcome the energetic barrier. The latter is associated to the reversible breaking/formation of chemical M−X bonds as well as to the electronic and ionic conducting properties of the precursors M_xX_y and generated Li-based ternary phases. From a literature survey of the entire conversion reactions so far reported[12] for whatever fluorides, oxides, sulfides, or phosphides coupled with our own experimental investigation, it turns out that the polarization ΔV is decreasing as we move from fluorides ($\Delta V \approx 1.1$ V) to oxides ($\Delta V \approx 0.9$ V), sulfides ($\Delta V \approx 0.7$ V), and phosphides ($\Delta V \approx 0.4$ V). This is fully consistent with the decrease in the M−X bond polarization from M−F to M−P. Therefore, a particular interest comes from the phosphides that react with Li over a narrow potential range, as reported by different groups. For instance, FeP_2[13] and CoP_3[14] reversibly react with Li at an average voltage of 1 V and show flat charge and discharge curves separated by ~0.4−0.5 V. However, their cycling performances were claimed to be very poor. More recently, Ti−P compounds, synthesized by the ball-milling method, were shown to present a capacity of ~900 mAh/g retained after 10 cycles.[15] Owing to the positive attributes of phosphides compared to oxides, except for the capacity retention, we decided to carry out a full electrochemical study of the binary M_xP_y phosphides family as reported herein. Through this exploratory survey of the 3d metal phosphides, the NiP_2 phase, which can crystallize either in a cubic or in a monoclinic form and which can be grown on a Ni-foam current collector, turns out to be quite an attractive negative material. The paper is organized as follows. An Experimental Section describes the synthesis and chemical/physical characterizations of NiP_2. Section 2 describes its electrochemical performance together with attempts at determining the reactivity mechanism as deduced by in situ X-ray, HRTEM (high-resolution transmission electron microscope) measurements, and electronic structure calculations. Finally, the design of a self-supported NiP_2 electrode for long cyclability application is reported as an improvement.

2. Experimental Section

XRD, TEM, and SEM. X-ray diffraction (XRD) measurements on powdered NiP_2 samples were performed on a Philips X-pert diffractometer using the Cu $K\alpha_1$ monochromatic radiation. A specifically modified scanning electron microscope Philips field effect gun (FEG) XL-30, as previously reported,[16] was used to carry out SEM (scanning electron microscope) studies on either Li-free or partially lithiated samples. A Tecnai F20 ST transmission electron microscope (TEM) equipped with EDS (energy-dispersive spectrometry) analysis was used to conduct our TEM/HRTEM investigations. To perform these experiments, the cells were stopped and opened in a drybox once cycled down to the required voltage. The partially lithiated material was recovered and washed with dimethyl carbonate (DMC) prior to being placed onto a copper grid mounted on our TEM sample holder. Through a special mobile airlock of our own design, the sample was then transferred to the TEM, without any air exposure, for selected-area electron diffraction (SAED) pattern and bright field image collection.

Electrochemical Tests. Swagelok-type cells were assembled in an argon-filled glovebox and cycled using a VMP or a Mac Pile automatic cycling/data recording system (Biologic Co, Claix, France) in a potential window between 2.5 and 2 and 0.02 V vs Li^+/Li^0 and a cycling rate of C/10 (that is 1 lithium per formula unit in 10 h). These cells comprise a Li-metal disk as the negative electrode, a Whatman GF/D borosilicate glass fiber sheet saturated with 1 M $LiPF_6$ in ethylene carbonate (EC), dimethyl carbonate (DMC) (1:1 in weight) as the electrolyte, and, unless otherwise specified, a positive electrode made by mixing the starting transition metal phosphides powder with 15% (weighed) carbon black (SP). Usually, 10−12 mg of the mixed powders were placed on top of the Swagelok plunger.

In situ XRD electrochemical cells assembled similarly to our Swagelok cell but with a beryllium window as current collector on

---

(7) Débart, A.; Dupont, L.; Patrice, R.; Tarascon, J.−M. *J. Mater. Chem.*, submitted for publication.

(8) Badway, F.; Cosandey, F.; Pereira, N.; Amatucci, G. G. *J. Electrochem. Soc.* **2003**, *150*, A1318−A1327.

(9) Gillot, F.; Monconduit, L.; Morcrette, M.; Doublet, M.-L.; Tarascon, J.-M. *Chem Mater.* **2005**, *17*, 3627.

(10) Hu, J.; Li, H.; Huang, X. *Electrochem. Solid-State Lett.* **2005**, *8*, A66.

(11) Pralong, V.; Leriche, J.-B.; Beaudoin, B.; Naudin, E.; Morcrette, M.; Tarascon, J.-M *Solid State Ionics* **2004**, *166* (3), 295.

(12) Tarascon, J.−M.; Grugeon, S.; Laruelle, S.; Larcher, D.; Poizot, P. Lithium Batteries − Science and Technology. In *Science and Technology of Advanced Lithium Batteries*, Nazri, G. A., Pistoia, G., Eds.; Kluwer Academic Publishers: Boston, MA, 2003.

(13) Silva, D. C. C.; Crosnier, O.; Ouvrard, G.; Greedan, J.; Safa-Sefat, A.; Nazar, L. *Electrochem. Solid-State Lett.* **2003**, *6*, A162.

(14) Alcantara, R.; Tirado, J. L.; Jumas, J. C.; Monconduit, L.; Olivier-Fourcade, J. *J. Power Sources* **2002**, *109*, 308. Pralong, V.; Souza, D. C. S.; Leung, K. T.; Nazar, L. *Electrochem. Comm.* **2002**, *4* (6), 516.

(15) Woo, S.; Sohn, H.-J. *IMLB 12 Meeting, Electrochem. Soc.* **2004**., Abs. 264.

(16) Orsini, F.; Du Pasquier, A.; Beaudoin, B.; Tarascon, J.-M.; Trentin, M.; De Beer, E.; Notten, P. *J. Power Sources* **1998**, *76*, 19.

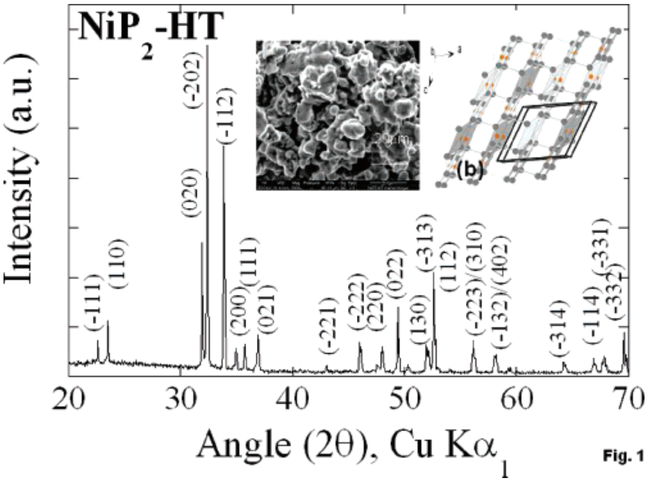

Figure 1. X-ray diffraction patterns (Cu $K\alpha_1$) of monoclinic NiP_2 prepared by a high-temperature ceramic route. Insets (a and b) show the SEM image and the NiP_2 monoclinic structure.

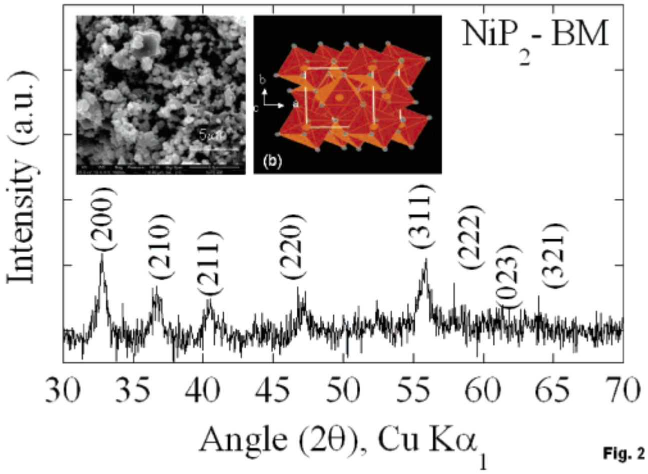

Figure 2. X-ray diffraction patterns (Cu $K\alpha_1$) of cubic NiP_2 prepared by a ball-milling route. Insets (a and b) show the SEM image and the NiP_2 cubic structure.

the RX side were placed on a Brucker D8 diffractometer (Co Kα = 1.790 26 Å) equipped with a PSD detector and connected to the VMP system. The cell was discharged at a C/10 rate, and the X-ray powder patterns were collected for every 0.1 reacted Li.

Electronic structure calculations were performed using both the extended Hückel tight-binding (EHTB) method and the first-principle density functional theory (DFT) using CAESAR[17] and VASP[18] codes, respectively. The former is used to give a qualitative picture of the molecular M_xP_y electronic structures, whereas the latter allows full structural relaxations and free electronic energy calculations.

3. Results

Synthesis. The monoclinic NiP_2 phase was synthesized at high temperature by placing stoichiometric amounts of nickel metal (Ni Alfa Aesar, 350 mesh, 99.9%) and red phosphorus (P Alfa Aesar, 100 mesh, 99%) powders in a sealed evacuated silica ampule.[19] The ampule was placed into a furnace, whose temperature was increased to 900 °C using a ramp of 20 °C/h, and held to this temperature for 5 days. The samples (denoted hereafter HT) were air-quenched.

Although the cubic NiP_2 phase was originally prepared at high pressure,[20] we succeeded in synthesizing it by room temperature ball milling (BM) with a Spex 8000 mixer-mill, as previously reported.[21] To prepare 1 g of NiP_2, stoichiometric amounts of Ni metal and red phosphorus powders were placed into a stainless steel container together with steel balls so that the powder-to-ball weight ratio ranged from 8:1 to 10:1. Through a survey of various grinding times, we experienced that the optimal ball-milling time to obtain single-phase powders was 8 h.

The XRD patterns of NiP_2−HT and NiP_2−BM powders are depicted in Figures 1 and 2. The results for NiP_2−HT reveal sharp Bragg peaks, indicative of a highly crystalline sample, which could all be indexed on the basis of a monoclinic cell with lattice parameters ($a = 6.38$ Å, $b = 5.62$ Å, $c = 6.08$ Å, $\beta = 126.22$, $C2/c$) similar to those reported in the literature.[19] Within the NiP_2 monoclinic unit cell, Ni is simply coordinated by P atoms in a nearly square-planar configuration. The structure can be viewed (right inset of Figure 1) as sheets of warped edge-sharing NiP_4 square-planes, connected to each other through short P−P distances (2.22 Å). A high degree of covalence is expected for the four Ni−P bonds of the square.

For the NiP_2−BM sample, the XRD powder pattern reveals weak Bragg peaks indicative of a poorly crystallized powder (Figure 2). All peaks are indexed in the *Pa*-3 (205) space group with $a = 5.4706$ Å cell parameter.[20] This pyrite-type NiP_2 phase is usually prepared by a high-pressure technique. The occurrence of this structure in the Ni dipnictides and its absence in the others (Fe, Cu, and Pd) has been explained in terms of electronic stability as derived from band-structure calculations.[20] Within the NiP_2 pyrite-type structure, the nickel atoms are in a trigonal-distorted octahedron surrounded by P atoms. The P atoms are in the form of a dianion that has the formal valence P_2^{4-}. The P−P distance is smaller than the sum of the normal tetrahedral covalent radii (1.10 Å, Pauling). The Ni−P distance is 2.29 Å, and the octahedral covalent radius of nickel is 1.23 Å.

Powder morphologies were investigated by SEM (left insets of Figures 1 and 2). In both cases, the powders are made of shapeless particles having an average size ranging from 5 to 50 μm for the NiP_2−HT sample and from 0.5 to 2 μm for the ball-milled NiP_2−BM sample. Both samples were highly conductive, consistent with their previously reported metallic behavior.[22]

Electrochemical Properties. Two Li/NiP_2−HT and Li/NiP_2−BM half-cells were assembled and tested for their electrochemical behavior at a *C*/10 rate. During the first discharge down to 0 V, the voltage composition curves for NiP_2−HT-based (Figure 3) and NiP_2−BM-based (Figure 4) Li cells show the insertion of 5.9 and 5.0 Li^+ per formula

---

(17) Ren, J.; Liang, W.; Whangbo, M.-H. Crystal and Electronic Structure Analysis Using CAESAR. http://www.primeC.com, 1998.
(18) Kresser, G.; Hafner, J. *Phys. Rev. B* **1993**, *47*, 558.
(19) Rundqvist, S. *Acta Chem. Scand.* **1961**, *15*, 451.
(20) Donohue, P. C.; Bither, T. A.; Young, H. S. *Inorg. Chem*. **1968**, *7*, 998.
(21) Takacs, L.; Mandal, S. K. *Mater. Sci. Eng.* **2001**, *429*, A304.
(22) Shirotani, I.; Takahashi, E.; Mukai, N.; Nozawa, K.; Kinoshita, M.; Yagi, T.; Suzuki, K.; Enoki, T.; Hino, S. *Jpn. J. Appl. Phys.* **1993**, *1*, 32.

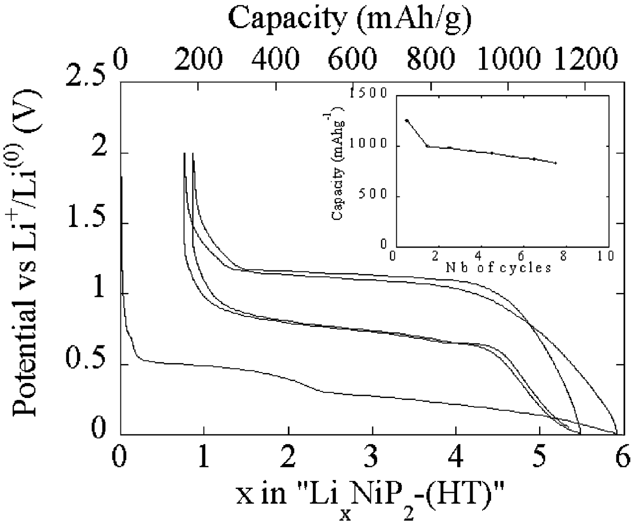

Figure 3. Composition−voltage profile for an HT-NiP_2/Li cell cycled at *C*/10 rate between 2 and 0V and its capacity retention as an inset.

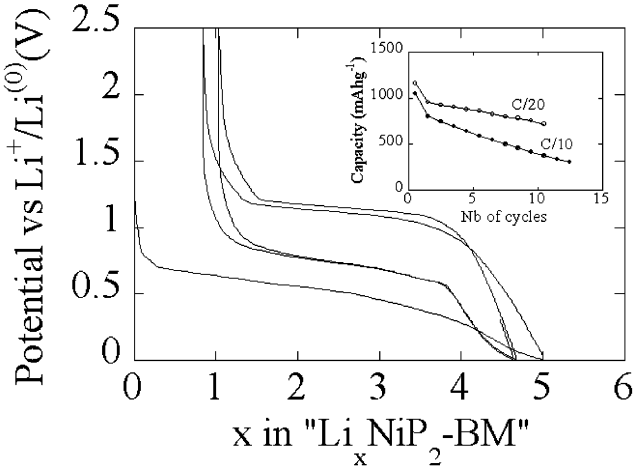

Figure 4. Voltage−composition curve for a Li half-cell, using a BM-NiP_2 sample as the positive electrodes and cycled between 2.5 and 0.1 V at a *C*/10 rate. The inset shows the capacity retention at two different regimes: *C*/10 and *C*/20.

unit, respectively. Upon recharge up to 2 and 2.5 V, only 5.0 Li^+ per formula unit can be removed from NiP_2−HT and 4.2 Li^+ from NiP_2−BM, leading to reversible capacities of 1000 mAh/g (4900 mAh/cm^3) and 840 mAh/g (4100 mAh/cm^3), respectively. Both cells show ∼16% capacity loss between the first discharge and the first charge and a capacity decay upon cycling that is worse for the Li/NiP_2−BM cell at a *C*/10 rate and pretty much the same at a *C*/20 rate (inset Figure 4). Therefore, the most striking difference between the two cells lies in the shape of the first discharge curve. For the Li/NiP_2−BM cell, after an initial Li uptake associated to the insertion of Li into the acetylene black, the voltage continuously and smoothly decreases down to zero volt, as is often observed in ball-milled electrodes. This is deeply contrasted with the discharge profile of the Li/NiP_2−HT cell that, besides the voltage hint associated to acetylene black, shows a well-pronounced voltage step near $x = 2.4$ that vanishes upon the subsequent discharges. Interestingly, except for the first discharge, both cells present the same charge/discharge voltage profiles upon subsequent cycles. The difference in the first discharge profile between the Li/NiP_2−HT and Li/NiP_2−BM cells suggests a different Li-reactivity mechanism, clearly linked to the different structural arrangements of both starting electrodes. To get deeper insights into these differences, both in situ XRD measurements and semi-in situ high-resolution transmission electron studies were performed.

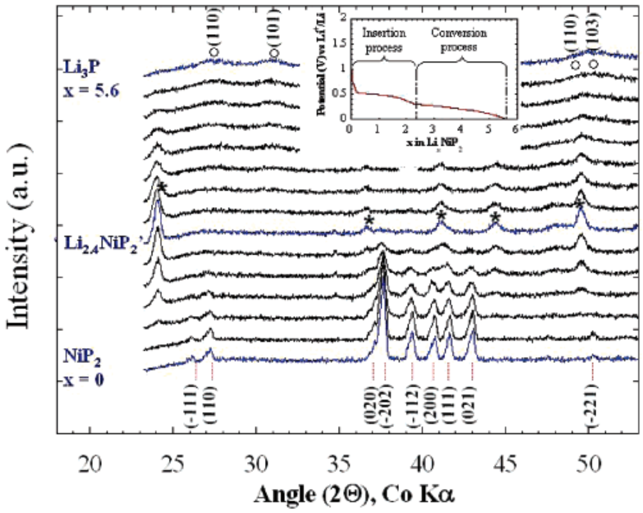

Figure 5. In situ X-ray diffraction patterns collected during the discharge of a NiP_2−HT/Li electrochemical cell down to 0.02 V at a *C*/10 rate (see inset). Bragg reflections are indexed for the mother phase, and the Bragg peaks corresponding to the A-phase (see text) and Li_3P phase are referred to by stars and empty cycles, respectively.

In situ X-ray Diffraction. As a NiP_2−HT/Li cell is discharged (Figure 5), we initially observed a continuous decrease in the intensity of the main NiP_2−HT Bragg peaks to the expense of a new set of Bragg peaks illustrated by stars on Figure 5. These peaks then grow upon increasing *x* to become unique at $x = 2.5$, indicative of a new phase denoted A having the formula $Li_{2.5}NiP_2$, and whose structure will be discussed below. Pursuing the lithiation results in the disappearance of the A-phase leads to the expense of a new set of broad peaks illustrated by circles on Figure 5 and corresponding to the hexagonal Li_3P.[23]

In contrast, when NiP_2−BM/Li is discharged, we only observe (Figure 6) a continuous decrease in the NiP_2−BM main Bragg peaks up to $x = 4.5$, with the appearance of broad peaks located at the Li_3P characteristic angles at the end of the reduction process.

When the two different cells are charged, similar XRD patterns are obtained for NiP_2−HT and NiP_2−BM. They are shown for the NiP_2−BM on Figure 7 a. They first show a progressive decrease in the Li_3P Bragg peaks and then a complete disappearance down to $x \approx 2$. The X-ray powder patterns for the fully charged samples show a broad and diffuse peak, characteristic of an amorphous electrode.

Upon subsequent cycles, both in situ X-ray cells show similar behaviors with, namely, the direct growth of Li_3P during discharge (presented here for NiP_2−BM Figure 7b) and its disappearance during charge. At first sight, this is indicative of a conversion reaction process ($NiP_2 + 6Li^+ + 6e^- \rightarrow 2\ Li_3P + Ni$). Note that, in both cases, we could not spot any signs of Bragg peaks corresponding to the growth

---

[23] Brauer, G.; Zintl, E. *Z. Phys. Chem., Abt.* **1937**, *B37*, 323.

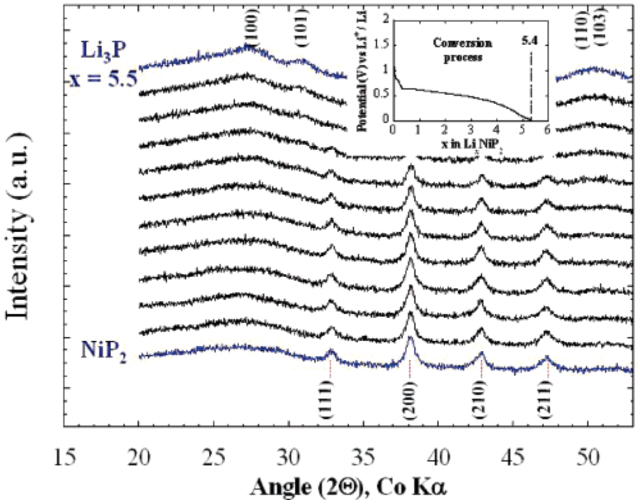

Figure 6. In situ X-ray diffraction patterns collected at various stages of discharge of a NiP$_2$−BM/Li electrochemical cell cycled between 0.01 and 2.5 V at a *C*/10 rate. *hkl*'s were used to represent the Bragg peaks corresponding to the NiP$_2$−BM phase (bottom) and to the Li$_3$P phase (top).

of metallic Ni. According to the in situ X-ray data, the formulation of the fully discharged composite electrode should be identical, independent of whether we have discharged a NiP$_2$−HT/Li or a NiP$_2$−BM/Li cell. Owing to such a similarity, the cells should then behave alike without showing any differences in capacity retention. At first glance, it would be tempting to explain this phenomenon in terms of powder morphology differences between the two samples. However, we cannot rule out volume consideration arguments to account for such a different capacity retention behavior, because the unit cell volume of a NiP$_2$−BM cubic cell is ~12 Å^3 lower than that of the NiP$_2$−HT monoclinic cell.

While the in situ X-ray data enabled us to pin down differences between the Li-reactivity mechanisms of NiP$_2$−HT and NiP$_2$−BM, with, namely, a hint of an insertion process followed by a conversion process for the former as compared to a single conversion process for the latter, it did not allow us to solve the structure of the A-phase and it failed to identify Ni particles expected for the conventional conversion reaction. An HRTEM study was undertaken in order to check the presence of Ni in the fully discharged samples and to provide a structural assessment for the A-phase.

HRTEM Study. The monoclinic NiP$_2$ powder is made of large ceramic particles with sharp edges that are a few microns long. A high-resolution TEM image (Figure 8) taken along the 001 zone axis (left inset) on a particle edge (right inset) shows that the particles are pretty well crystallized with no obvious fault. EDS analyses were performed on this sample in order to standardize the nickel/phosphorus ratio.

To identify the intermediary A-phase, a NiP$_2$−HT/Li cell was discharged down to $x = 2.5$, and, once recovered, the Li$_{2.5}$NiP$_2$ electrode was examined by TEM. While a random intergrowth between two phases was first suspected on the bright field images (not shown), the high-resolution image taken at the interface between two regions (Figure 9a) showed that the second phase does not exist from a crystallographic point of view but is the result of stacking faults piling up between two consecutive well-crystallized regions. The corresponding SAED pattern (Figure 9b) confirms this observation, since well-defined spots induced by a well-crystallized phase as well as diffuse lines resulting from stacking faults are observed.

An electron diffraction study was carried out to determine the cell parameters of the phase responsible for the crystallized regions. From the set of dots recorded on several SAED patterns from the same crystal and from several particles, we succeeded in building the reciprocal space (Figure 9c). A tetragonal cell could then be proposed as a rough estimate: $a = 5.5$ Å and $c = 4.2$ Å. Such a cell can be easily deduced from the initial monoclinic NiP$_2$−HT cell. As shown on Figure 10a, Li insertion in the interlayers region should lead to the breaking of the short P−P bridges, favoring an easy gliding of all adjacent sheets and, therefore, a closing of the monoclinic β angle. This could explain the nearly orthogonal angle found for the tetragonal cell. Simultaneously, a square planar to pseudo-tetrahedral distortion occurs in the NiP$_4$ entities to minimize the P−P repulsions induced by the exceeding charge on the phosphorus. This

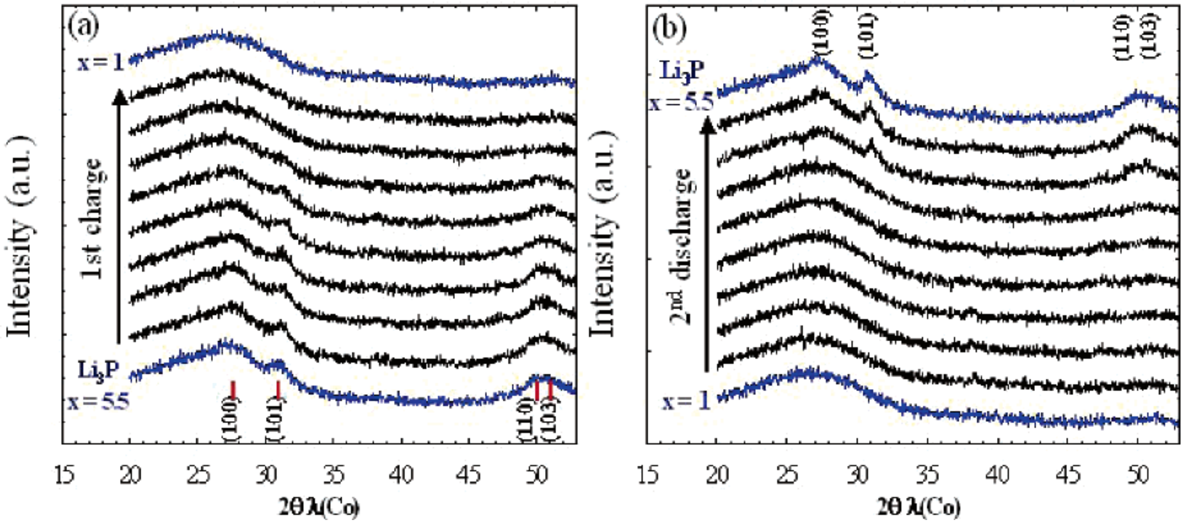

Figure 7. In situ X-ray diffraction patterns collected at various stages of (a) charge of a NiP$_2$−BM/Li electrochemical cell cycled between 0.01 and 2.5 V at a *C*/10 rate and (b) a second discharge of the same electrochemical cell.

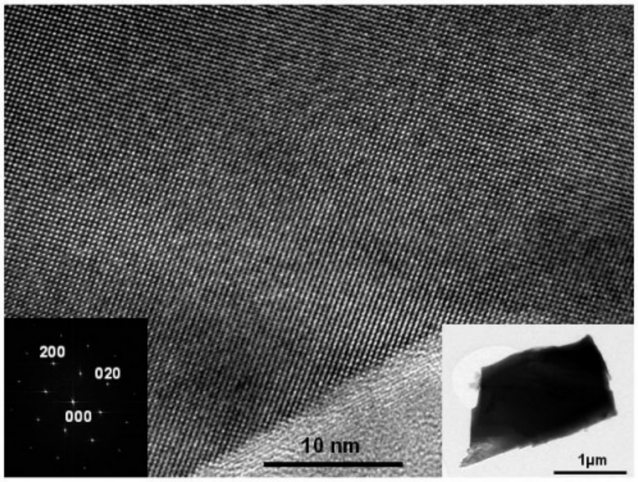

Figure 8. HRTEM image realized on the edge of a monoclinic NiP_2 particle (right inset) along the 001 zone axis according to the electron diffraction pattern (left inset).

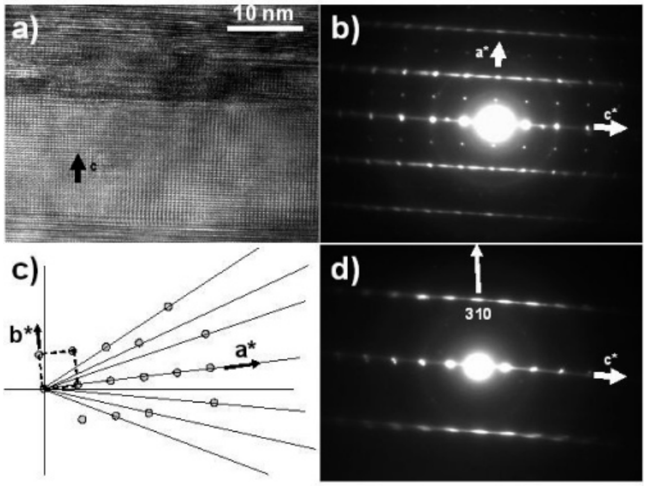

Figure 9. TEM study of partially discharged monoclinic NiP_2 of $Li_{2.4}NiP_2$ composition. (a) High-resolution image showing random intergrowth of disordered domains, (b) corresponding SAED pattern, along the 010 zone axis, (c) scheme showing the reciprocal space reconstruction (experimental dots are in green (plain), while extrapolated ones are open in blue), and (d) SAED pattern along the 1-30 zone axis.

should disconnect the NiP_4 square planes from each other in at least one direction, leading to Ni_2P_4 chains of edge-sharing distorted tetrahedra. This new linkage mode is not only necessary to compensate the lack of P-atoms induced by the in-plane rearrangement but also appears to be the most plausible local distortion to explain the unit cell parameters measured from HRTEM. In this novel lamellar packing, one can easily link the periodic Ni−Ni distances to the translation vectors of the pseudo-tetragonal phase, i.e., $a \approx b = 5.5$ Å and $c = 4.2$ Å. This picture is consistent with the electronic structure calculation performed on the NiP_4 square plane given in Figure 10c, which shows that the phosphorus atoms are the redox centers in the NiP_2 monoclinic structure. Indeed, the splitting of the metallic 3d orbitals in the D_{4h} local symmetry leads to four quasi-degenerated metallic-like orbitals well-separated in energy from the fifth metallic orbital by several P-like levels. In such a configuration, the transition metal is d^8 (i.e., Ni^{+II}) yielding the $Ni^{+II}(P^-)_2$ general formulation. This is completely different from the NiP_2 cubic structure in which the octahedral metallic environment leads to a d^6 electronic configuration, i.e., $Ni^{+IV}(P^{2-})_2$ and, therefore, to an obviously different redox mechanism (Figure 10d).

To get a better insight into the structural aspects linked to the existence/growth of the $Li_{2.5}NiP_2$ phase, we further processed the recorded SAED patterns. In carrying out meticulous measurements, we realized that the "tetragonal cell" (used to index Figure 9 parts b−d) should not be considered as a real cell but rather as a subcell. Indeed, the 001 zone axis electron diffraction pattern (not shown here) shows that *a* and *b* cell parameters are slightly different while the [1−30]* zone axis SAED pattern (Figure 9d) gives evidence of a monoclinic cell rather than a tetragonal one, since the [310]* and [001]* directions are not perpendicular. We are currently investigating the $Li_{2.5}NiP_2$ monoclinic cell parameters by combining these results with recorded XRD patterns using pattern matching.

Returning to Figure 9a, we determined that the coexistence of well-crystallized domains parted from disordered ones is most likely the signature of local composition changes associated either to (1) difficulties encountered in reaching equilibrium during sample preparation or (2) the advent of a second Li-driven reaction, because we exceed values of *x* corresponding to the existence of the A-phase. The fact that the same observations were made on samples discharged up to $x = 2.2$ only and at rates as slow as *C*/100 led us to conclude that we are dealing with a highly unstable phase. Consequently, it is quite possible that, for *x* values close to the limit *x* value, there is a competition between the end of the Li insertion process and the beginning of the conversion reaction process as described hereunder. Evidence of such initiation of the conversion process was brought about by the spectacular collapse of the structure (Figure 11) associated to the release of Ni particles (inset Figure 11).

Moving to the end of the discharge process, agglomerates containing nanoparticles as well as a huge quantity of polymeric coating are observed (Figure 12a inset). Owing to the rapid evaporation of the polymer coating under the beam, difficulties were encountered in initially collecting highly contrasted images (see Figure 12a). Therefore, after a long time of exposure, crystallized 5 nm particles identified from the corresponding SAED pattern (inset Figure 12b) as Ni particles are nicely observed (Figure 12b). Contrary to the XRD results, Li_3P reflections are not easily observed on the corresponding SAED patterns. Such a different behaviour could be nested in an enhanced solubility of the Li_3P into the polymer electrolyte so that, when the polymer evaporates under beam exposure, it takes away a part of the Li_3P, leaving mainly nickel nanoparticles on the edge of the agglomerates where the TEM observation is done.

Finally, bright field images of the fully recharged sample (cell cutoff voltage fixed to 2 V) indicate that it is quite heterogeneous with agglomerates either surrounded by (Figure 13 parts a and b) or free from polymeric coating (Figure 13c). High-resolution images (Figure 13d) taken on these aggregates indicate that their cores are amorphous while their edges are crystallized (lattice fringes are observed on 5−10 nm wide domains). According to the fast Fourier transformation (FFT) calculated on the HRTEM images

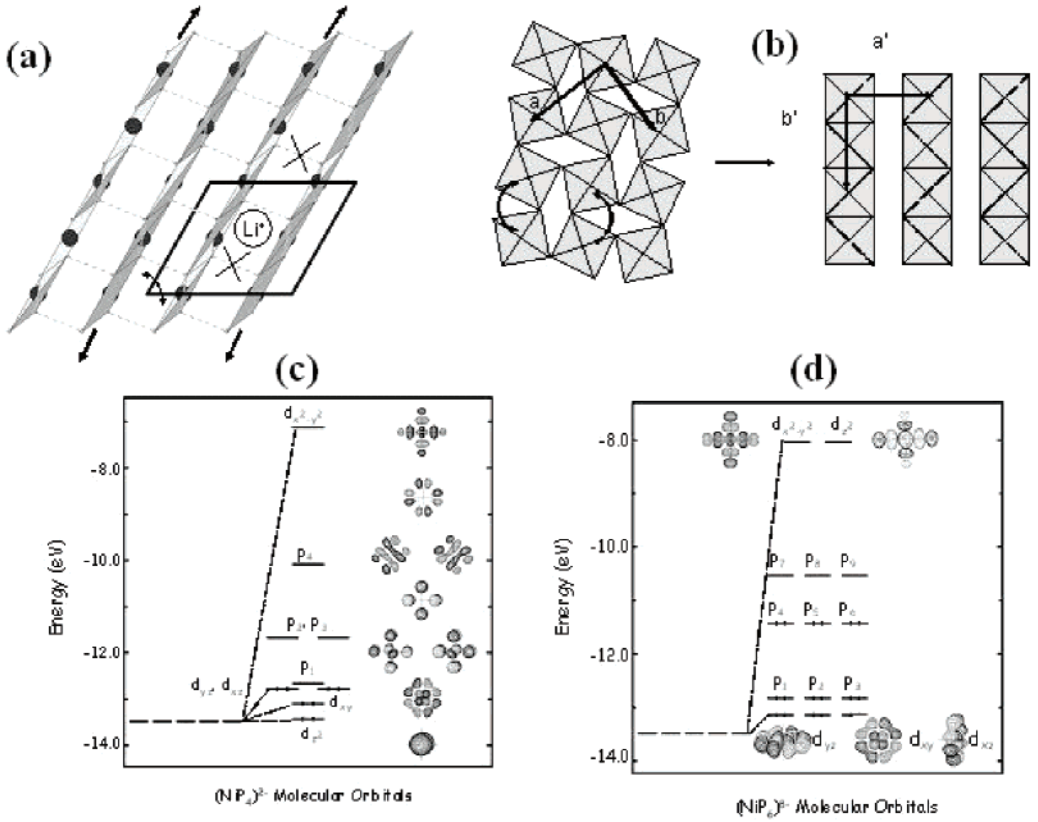

Figure 10. Structural rearrangements involved in the NiP_2 monoclinic structure (a) in the interlayers and (b) in the layer planes to form the Li_xNiP_2 tetragonal phase (black circles represent the Ni atoms, and small gray circles represent the P atoms). The extended Hückel tight-binding (EHTB) electronic structures are shown for (c) NiP_4-type environments (square plane) and (d) NiP_6-type environments (oactahedra).

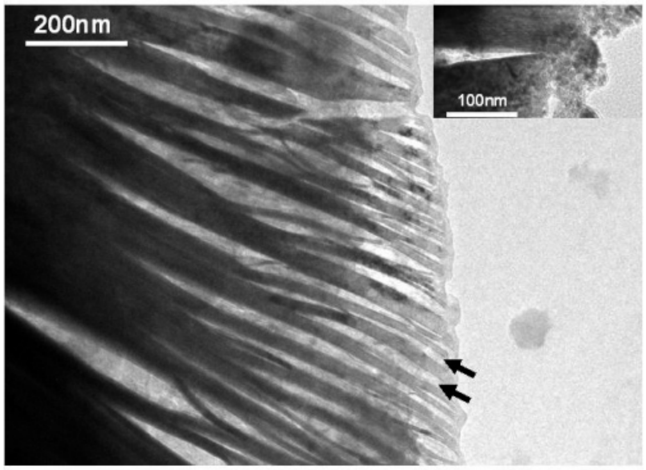

Figure 11. Bright field TEM image showing the alternation of collapsed domains (dark arrows) with layered A-phase domains. Inset: enlarged image showing the formation of nanoparticles at the edge of the domains.

(inset Figure 13d), measured inter-reticular distances were assigned to 110, 200, or 021 NiP_2 reflections. According to the electrochemical data, the process is nearly fully reversible; therefore, an intriguing question yet to be answered is why only part of the reformed NiP_2 is crystallized?

Finally, to throw some light on the electrochemical behavior differences between the cells using either NiP_2−HT or NiP_2−BM as the positive electrode, our TEM study was extended to materials recovered from partially discharged/charged cubic NiP_2−BM/Li cells. TEM images collected for the fully discharged cubic NiP_2−BM phase were similar to the ones observed for the fully lithiated monoclinic NiP_2−HT. They show both the polymeric coating vanishing under the beam and the occurrence of nanoparticles. Therefore, in opposition to the previous case, the nanograins were amorphous and, consequently, could not clearly be assigned to metallic nickel. The fully charged cubic NiP_2−BM sample (at 2.5 V) is made, as before, of agglomerates of amorphous nanoparticles that neither high-resolution images nor SAED patterns could clearly identify.

4. Discussion

The previously discussed results show that both the monoclinic NiP_2−HT and the cubic NiP_2−BM phases behave similarly once the first discharge is fully achieved. NiP_2−HT is reduced by Li through a two-step process enlisting first the insertion of Li into NiP_2 to give a $Li_{2.4}NiP_2$ phase and second the conversion of $Li_{2.4}NiP_2$ into a composite made of Li_3P and Ni° nanoparticles. For NiP_2−BM, in contrast, a single reaction path was observed. Although no clear evidence of Ni° nanoparticles was observed in the fully discharged sample, the direct conversion of NiP_2 into Li_3P and Ni° is suggested. Usually, for the conversion reactions so far reported either with oxides, sulfides, or fluorides, the measured amount of Li uptake during the first discharge was always greater than the theoretical one. The extra capacity was associated either to a reversible growth of an electrochemically gellike polymer layer or to a reversible, heterogeneous interfacial storage mechanism.[24] Presently, whatever the structure of the NiP_2 precursor phase, the measured amount of Li uptake per formula unit (5.9 and 5 for monoclinic and cubic NiP_2,

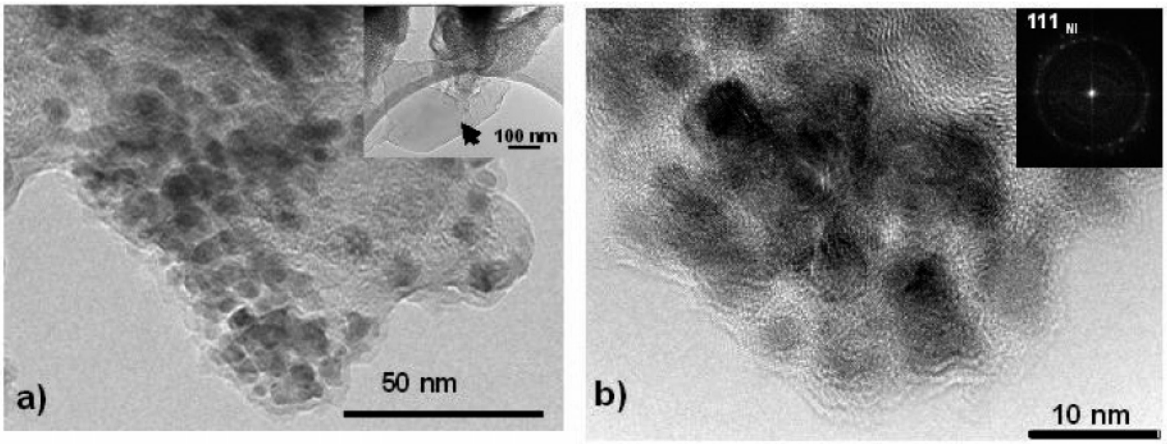

Figure 12. Bright field images recorded on a fully discharged monoclinic NiP_2−HT sample. The a and b sequence corresponds to an increase in magnification as well as beam exposure time. (a) Dark arrow on the inset shows the polymeric layer vanishing under the beam, and then continuous disappearing of Li_3P/polymeric layer is observed, and (b) high-resolution image of nickel nanoparticles together with an FFT in inset.

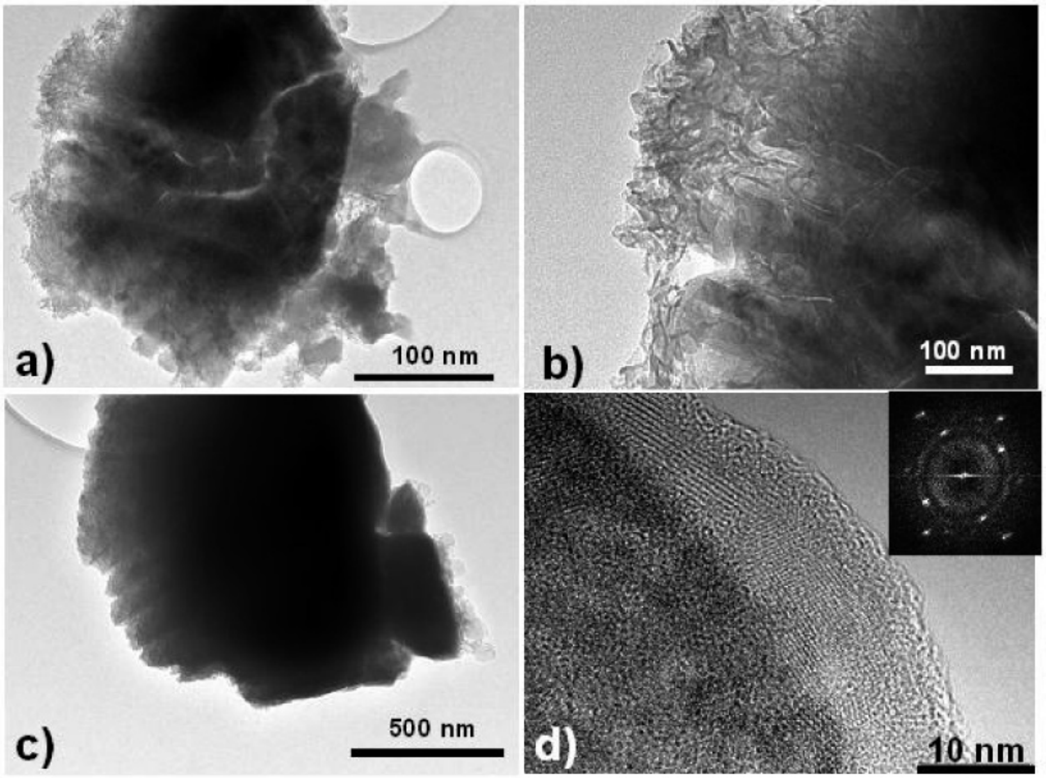

Figure 13. TEM images recorded on a fully recharged monoclinic NiP_2−HT sample up to 2 V. (a) Some agglomerates are still surrounded by a thick polymeric coating, (b) enlarged image, (c) high-resolution image, and (d) high-resolution image of monoclinic NiP_2 together with an FFT in inset.

respectively, carbon accounted) never reaches the value of 6 expected for the complete conversion reaction $NiP_2 + 6Li \rightarrow 2\ Li_3P + Ni^{\circ}$, even though we gave evidence, as deduced from HRTEM, of the formation of a polymeric layer. This result came as a surprise, and in an attempt at rationalizing it, we checked the effect of the discharge cutoff voltage on the amount of Li uptake during the first discharge. Even by pushing the discharge down to voltages where we observed the onset of Li plating, we did not succeed in getting Li uptake values >6.2 per formula unit. Although we do not have a sound, straightforward explanation to account for the specific behavior of phosphides toward conversion reactions, we suppose that it has to do with the feasibility of having anionic redox centers as opposed to cationic redox centers only, as with the other compounds we have so far investigated.

Another universal characteristic of the conversion reactions so far studied is the existence of a large potential difference between the first and second discharge, the latter being always a few 1/100ths of a mV above the first. The larger drop in potential observed during the first discharge can be viewed as the necessary potential to provide the required activation energy to trigger the conversion reaction. Once this formation step is achieved, thanks to the nano-character of the formed composite, the second discharge will be kinetically less limited and, hence, will show an increase in

---

(24) Maier, J. "Nano-Ionics": Ion Transport and Electrochemical Storage in Confined Systems. *Nature Mater.* **2005**, submitted for publication.

the discharge voltage. The phosphides are no exception to this phenomena, since a $\Delta V = 0.3$ and 0.5 V is observed between the first and second discharge for NiP$_2$−BM and NiP$_2$−HT, respectively.

To explain the different mechanisms involved in the first discharge, first-principle electronic structure calculations have been performed on the cubic and the monoclinic NiP$_2$ as well as on Li$_3$P and Ni-metal. Very close free electronic energies are computed for the two fully relaxed systems, with the cubic phase being thermodynamically more stable than the monoclinic phase by no more than 25 meV per unit cell. These close energies would suggest equivalent equilibrium potentials for the $NiP_2 + 6Li \rightarrow 2\ Li_3P + Ni°$ conversion reaction, as corroborated by the enthalpy of reaction (ΔG) per Li atom computed for the two starting electrodes ($\Delta G_{mono} = -0.897$ eV and $\Delta G_{cub} = -0.893$ eV). The different potentials observed in the first discharge voltage curves of NiP$_2$−HT and NiP$_2$−BM clearly correspond to different redox mechanisms associated with different Ni oxidation states and local environments. As shown by EHTB electronic structure calculations, the splitting of the metallic 3d orbitals in the D_{4h} (square-planar) and in the Oh (octahedral) symmetry induces a Ni^{+II} (d^8) and a Ni^{+IV} (d^6) oxidation state, respectively. On one hand, the NiP$_2$ cubic form can be easily deduced from the monoclinic form by a slight interlayers contraction, consistent with the high-pressure synthetic conditions. On the other hand, the NiP$_2$ monoclinic form can be deduced from the cubic form by a Jahn Teller-type distortion, easily consistent with a nonstable d^8 octahedral environment. The closely packed structure of the cubic NiP$_2$ prevents any lithium insertion, thus favoring a direct conversion reaction into Li$_3$P and Ni°. In contrast, the monoclinic NiP$_2$ exhibits some available interlayers space to accommodate lithium ions, hence enabling the formation of the monoclinic Li$_{2.5}$NiP$_2$ phase. More precisely, if we accounted for the Li insertion into the SP-carbon added to the electrode, the stoichiometry of the monoclinic phase is near Li$_2$NiP$_2$.

The break in the voltage−composition trace for NiP$_2$−HT/Li cells discharged at very low rates (*C*/20) revealed the existence of the intercalated Li$_2$NiP$_2$. Therefore, by increasing the discharge rate to values approaching *C*/5, we observed a smoothing of the discharge curve. In light of such findings, a legitimate question is whether the absence of a step-voltage anomaly in the voltage−composition trace for NiP$_2$−BM/Li cells is simply the result of a poorly selected discharging rate. To check this point, we discharged a NiP$_2$−BM/Li cell at a *C*/100 rate and still observed a smooth voltage−composition trace, providing irrefutable proof that both NiP$_2$ polymorphs react differently toward Li.

Nevertheless, whatever the first discharge reacting paths for both cubic and monoclinic NiP$_2$, we have shown, as deduced by HRTEM, that they are leading composition-wise to a somewhat identical fully discharged electrode material made of Li$_3$P and Ni° nanoparticles (the latter being amorphous for NiP$_2$−BM and crystallized for NiP$_2$−HT). Once the first discharge is achieved, electrochemical data further stressed the similarity between both NiP$_2$ polymorphs, owing to the superimposition of the voltage/composition traces or of their derivatives (Figure 14) over the next charging/discharging cycles. Therefore, once the cycling is extensively pursued, such a similarity no longer holds, since the capacity was shown to decay quite more rapidly for cubic NiP$_2$ as compared to monoclinic NiP$_2$. Among the most common reasons to account for capacity decays upon cycling are (i) the presence of particles becoming electrically disconnected and (ii) the onset of secondary reactions enlisting a slight instability of the phosphorus-based reaction products with the present electrolyte, leading to some decomposition. Since electrolyte decomposition reactions catalyzed by electrode materials are known to be enhanced by defects and large surface areas, one would expect these reactions to be more pronounced for the NiP$_2$−BM powders that are of poor crystalline nature and highly divided as compared to the bulky and highly crystalline NiP$_2$−HT powders. On that basis, the largest capacity fading observed for the ball-milled NiP$_2$ powders does not come as a surprise.

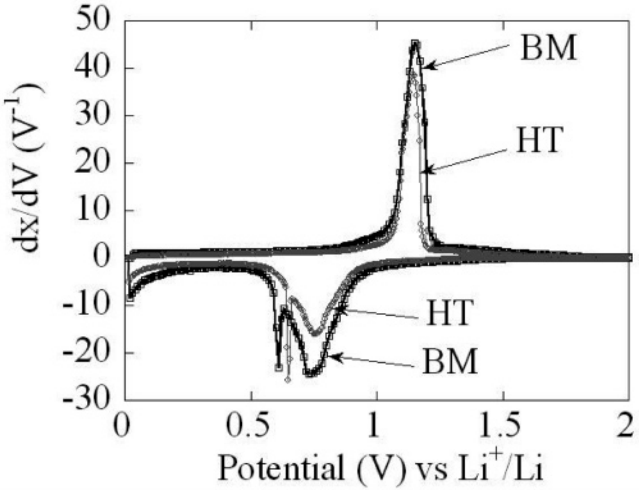

Figure 14. Derivative d*x*/d*V* plots are shown for the fifth cycle for two BM-NiP$_2$/Li and HT-NiP$_2$/Li cells cycled at a *C*/10 rate between 2 and 0.01 V.

Although the capacity retention in NiP$_2$−HT is better, it still falls short of being suitable for practical applications. Besides, both polymorphs show limited rate capabilities since only 60% of the initial capacity can be recovered at a *C* rate. Such negative aspects should, therefore, not overshadow the main attributes of binary phosphides over binary oxides for conversion reactions, which are as follows: (i) a considerably lower polarization between charge and discharge voltage upon cycling (0.4 V instead of 0.8 V) leading to a better cycling efficiency, (ii) lower irreversibility loss during the first cycle (15 to 16% as compared to the 25−30% for the oxides), and (iii) a high reversible capacity (1000 mAh/g) at an average potential close to 1 V, which is high enough to avoid Li plating and low enough to not penalize the output voltage too much. On the basis of our cumulative experience with conversion reactions within the field of oxides, we felt confident that solving the poor capacity retention and rate capability problems, observed for NiP$_2$ and most likely associated to the poor electronic/ionic conductivity of the formed composite electrode and, hence, interfacial issues, was not an insurmountable task, as our first approach indicated.

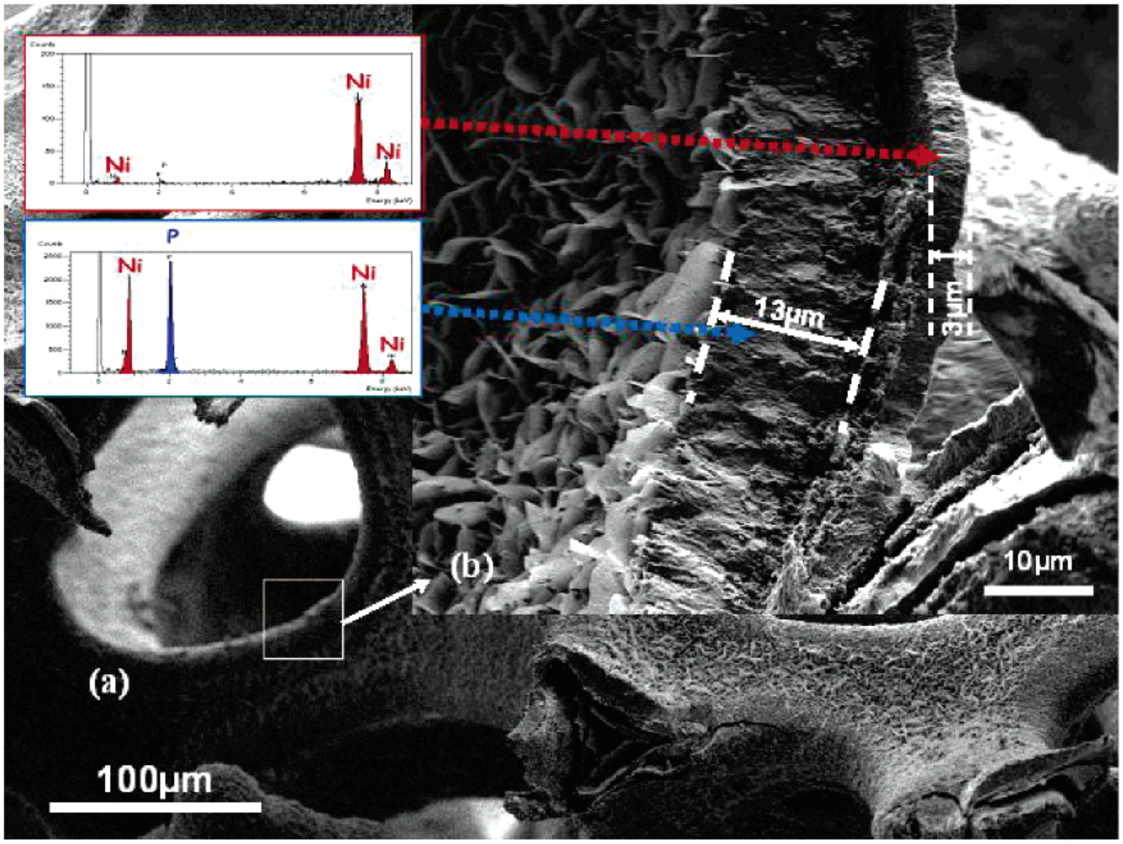

Figure 15. SEM images of a Ni-foam reacted with P, according to the conditions described in the text (12 h and 350 °C), are shown. (a) The pores of the Ni-foam recovered by NiP_2 are shown. (b) Enlarged image nicely showing the growth of the NiP_2 phase until reaching the Ni current collector, as deduced by the corresponding EDS analysis and nano sheet morphology of the obtained NiP_2.

Improving NiP_2 Electrode Performance. Such issues are quite common within the field of energy storage. For instance, to overcome the poor conductivity of the $Ni(OOH)_2$ electrode used in Ni-based batteries,[25] researchers have introduced Ni-foam to either physically (immersion of the electrode with the $Ni(OOH)_2$/carbon/binder paste) or chemically (electrodeposition of $Ni(OH)_2$ into the Ni-foam) host and, therefore, confer to the system high-power rate capabilities. Within the same spirit, Brousse and co-workers have succeeded in growing Cu_3P and Ni_2P on Cu and Ni metallic foils; see refs 26 and 27, respectively. In this study, we have explored the growth of NiP_2 onto Ni-foam, as described next.

Ni-foams purchased from Recemat (RCM-Ni-4852.016) were disposed in one compartment of a two-compartment evacuated-and-sealed quartz ampule with, in the other compartment, stoichiometric amounts of red phosphorus powders. A survey of various temperatures (ranging from 300 to 700 °C) and reaction times (2−120 h) was conducted. The quartz vessels were placed into an oven; once the selected annealing temperature profile was completed, the oven was turned off, the tube was opened, and the Ni grid was recovered for X-ray analysis and both SEM and EDS characterization. High-temperature treatments (650 °C) produced the monoclinic NiP_2 ($a = 6.38$ Å, $b = 5.62$ Å, $c = 6.08$ Å, $\beta = 126.22$, $C2/c$), but the Ni-foam was fully consumed, losing its mechanical integrity. In contrast, we experienced that, for annealing temperatures <300 °C, we could not obtain the NiP_2 phase independent of the reacting time. Thus, to tune the thickness of the grown NiP_2 phase to that of Ni, we fixed the annealing temperature at 350 °C and varied the reacting time from 2 to 120 h. The NiP_2 monoclinic phase formed (Figure 15) with times >2 h (as deduced by XRD), and the NiP_2 thickness layer (as deduced by SEM, Figure 15 b) increased with time to reach values of 3−4 μm after 6 h, 7−20 μm after 12 h, and exceeding 20 μm for longer times. An example of SEM observation of a treated Ni-foam (Figure 15b) clearly shows the growth of porous and flaky NiP_2 layers from metallic nickel, indicative of a good chemical interface. The film surface presents a layered crystallized morphology (Figure 15b). The heat-treated foams were electrochemically tested in Li half-cells. The best performances were obtained for those treated at 350 °C for 6 and 12 h with, namely, the reversible insertion of 5.4 and 5.2 Li per NiP_2, respectively. Therefore, the most important finding lies in the capacity retention of such electrodes, which outperforms what has been achieved so far from classical electrode preparation (Figure 16). Once the first cycle is achieved, note that the NiP_2-loaded Ni-foam sustained >90% of its capacity after 10 cycles (Figure 16 left inset), slightly better than that of the powder (Figure 3). Besides, such electrodes also show better rate capabilities, since they can deliver 92% of their initial capacity at a *C* rate (Figure 16 inset right).

---

(25) Ho, K. C.; Jerne, J. *Electrochem. Eng. Appl*. **1987**, *83*, 254.

(26) Pfeiffer, H.; Tancret, F.; Bichat, M.-P.; Monconduit, L.; Favier, F.; Brousse, T. *Electrochem. Commun*. **2004**, *6*, 3, 263.

(27) Pfeiffer, H.; Tancret, F.; Brousse, T. *Mater. Chem. Phys.* **2005**, *92*, 534.

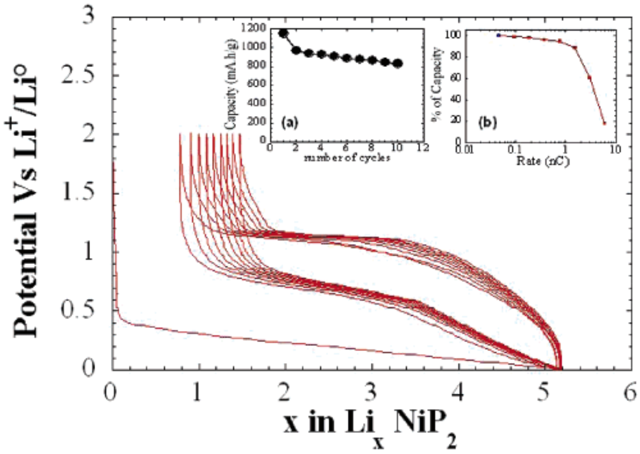

Figure 16. Composition−voltage curve for the foam-NiP_2/Li cell at *C*/10 from 2 to 0 V at a *C*/2 rate with, as inset, (a) its corresponding capacity retention. The second inset (b) shows the rate capability performance of a foam-NiP_2 electrode measured, for reasons of current density associated to Li-metal, in a Li-ion-type configuration using $LiFePO_4$ as the positive electrode.

Needless to say, further optimization work remains to be done; therefore, such results are very encouraging and help in building confidence in the possible use of phosphides in the next generation of Li-ion cells.

5. Conclusions

We have reported the electrochemical reactivity of two NiP_2 polymorphs (cubic and monoclinic) toward Li. The monoclinic form turns out to exhibit the largest capacity since it reversibly reacts with 5.0 Li per unit formula compared to solely 4.2 for the cubic form. Although the first discharge vs Li of the two polymorphs was enlisting different reacting paths, it turns out that the fully discharged materials were alike composition-wise and were made of Li_3P and Ni nanoparticles. From complementary XRD and HRTEM, we could unambiguously deduce that, on the subsequent cycles, both polymorphs were reacting with Li according to the following conversion process ($NiP_2 + 6\ Li^+ + 6e^- \rightarrow Ni^\circ + 2\ Li_3P$). To our knowledge, NiP_2 is among the first phosphides so far reported to react with Li through a full conversion process. In comparing with other phosphides, the attractiveness of NiP_2 does not lie on its large reversible capacity, which is shared by other binary (FeP_2) or ternary phosphides (Li_9TiP_4),[28] but rather on its ability to sustain 90% of its capacity over 15 cycles as well as on its aptitude to deliver its full capacity at 0.5*C*. The promises provided by this material were further exploited by confectioning a new electrode configuration within which the NiP_2 phase is directly grown on a Ni-foam. Using such a trick, we could obtain carbon-free, self-supported nickel diphosphide electrodes capable of sustaining high capacities over many cycles while having enhanced rate capabilities. We hope that this new electrode design approach will help to pave the way toward the optimization of binary phosphides such as FeP_2, which were abandoned despite their large initial capacity because of a very poor capacity retention. However, it should be noted that, although the elaboration of electrodes chemically combining the current collector (Ni) and the active material (NiP_2) did improve the capacity retention, there is still space for improvement. We believe that further work needs to be done at the electrolyte level aimed toward a better understanding of the secondary reactions linked to the electrolyte compatibility with phosphorus-based electrode materials. Implementation of this work toward the elaboration of other self-supported binary phosphides electrodes and their behavior in various classes of electrolytes is presently being conducted.

CM051574B

---

(28) Gillot, F.; Bichat, M. P.; Favier, F.; Morcrette, M.; Doublet, M.-L.; Monconduit, L. *Electrochim. Acta* **2004**, *49*, 2325. Bichat, M. P.; Gillot, F.; Monconduit, L.; Favier, F; Morcrette, M; Lemoigno, F.; Doublet, M.-L. *Chem. Mater.* **2004**, *16*, 1002.